scientific reports

Check for updates

OPEN

Oxygen-depleted and ferruginous seawater composition imprinted in Early Cretaceous Fe-rich Al-glauconites in marginal marine deposits

Arpita Chakraborty[1], Ayush Srivastava[1], Brijesh Singh[1], Jahnavi Punekar[1], Sudipta Dasgupta[1], Snehasis Chakrabarty[2] & Santanu Banerjee[1]✉

The composition of marine authigenic iron silicates bears subtle evidence of paleo-oceanographic and paleoclimatic conditions. This study focuses on the compositionally unique glauconite within the Early Cretaceous Pariwar and Habur formations in the Jaisalmer Basin and discusses its implications. The Al-glauconite is enriched in TFe_2O_3 (> 18 wt%), and is considered as Fe-rich Al-glauconite. The X-ray diffraction parameters, the micro-texture, and the K_2O content reveal an evolved to highly evolved structure of the glauconite. It is abundant in shallow subtidal and tidal- and wave-influenced shoreface facies, and it forms either by the alteration of fecal pellets or as bioclast infillings. Micropaleontological and ichnological proxies confirm the glauconitization in an oxygen-depleted, shallow marine depositional setting. Small-sized (< 1 cm) fodinichnial, pascichnial, domichnial, and repichnial traces, and agglutinated foraminifera (*Bathysiphon)* corroborate the oxygen-depleted seawater. The landward expansion of the oxygen minimum zone, leading to oxygen depletion in coastal settings, facilitates the glauconitization in a marginal marine setting. Kaolinite and Fe-Al-smectite react in the presence of excess Fe, forming Fe-rich Al-glauconite on the seafloor. Therefore, the compositionally unique glauconite reflects atypical seawater chemistry with increased elemental influx of Al, Fe, and Mg related to intense continental weathering, kaolinite substrate, and mobilization of Fe^{2+} in oxygen-depleted seawater.

Keywords Fe-rich Al-glauconite, Marginal marine, Oxygen depletion, Sequence stratigraphy, Ichnology, Agglutinated foraminifera

Glauconite primarily forms in modern oceans, mainly in the outer shelf to upper slope[1,2]. However, its ancient counterparts occur in wide-ranging environments[2–6]. Shallow marine glauconite is particularly abundant in the Late Cretaceous and Paleogene[2,6–9]. The warming events during these Periods favour glauconite-rich sedimentary deposits in shallow marine environments[2,10–12]. However, Early Cretaceous glauconites are rarely found in shallow marine to deltaic deposits[13,14]. The origin of shallow marine, Early Cretaceous glauconites remains poorly understood, as depositional conditions are rarely constrained by integrated sedimentological, ichnological, and micropaleontological data. A few studies have indicated that unusual seawater chemistry facilitates shallow marine glauconitization, but without much elaboration[15,16]. Shallow and deep marine glauconites differ compositionally; the former is typically enriched in Al_2O_3 and depleted in TFe_2O_3, while the latter contains high TFe_2O_3 and low Al_2O_3[2,17]. The high alumina glauconite or Al-glauconite, with Al_2O_3 content > 10 wt% is commonly reported from shallow marine environments, in which the TFe_2O_3 content rarely exceeds 18 wt%[18].

This study focuses on the mode of occurrence and the formation mechanisms of Early Cretaceous glauconites in the Mesozoic Jaisalmer basin. Although a few studies explore the depositional history of the Jurassic succession of this basin, the Cretaceous interval is largely overlooked. Lithostratigraphy, plant fossils, and nanoplankton of the shallow marine Cretaceous Jaisalmer basin are described in some studies[19–21]. Although glauconite is

[1]Department of Earth Sciences, Indian Institute of Technology Bombay, Powai, Mumbai 400076, India. [2]KDMIPE, Oil and Natural Gas Corporation Ltd., Dehradun 248195, India. ✉email: santanu@iitb.ac.in

abundant across the Cretaceous[2], detailed geochemical analysis is lacking for the Early Cretaceous glauconites. Further, micropaleontological and ichnological proxies have been rarely used for estimating depositional redox conditions. Although glauconite has been completely overlooked in outcrop, a few reports indicate its occurrence in subsurface Early Cretaceous deposits[19,22]. Since glauconite is a useful marker for stratigraphic correlation, and its composition is sensitive to depositional conditions, an integrated sedimentological, ichnological, and micropaleontological study is likely to constrain the depositional conditions during glauconitization. The objectives of this research are (i) to understand the origin of the Early Cretaceous marginal marine glauconite, and (ii) to explain the link between glauconite composition and depositional conditions and highlight the unique characteristics of Early Cretaceous glauconite.

Geological background

The Jaisalmer Basin, a pericratonic rift basin at the northwestern margin of peninsular India, separated from Gondwanaland during the Late Triassic[23,24], extending across the India-Pakistan border as the Indus Shelf[19,23]. The basin has four major tectonic units: Kishangarh shelf in the northwest, Jaisalmer-Mari High in the center, Shahgarh low in the southwest, and Miajlar low in the southern part of the basin[19,25]. The Cretaceous succession of the Jaisalmer Basin comprises Pariwar and Habur formations in the outcrop and Pariwar, Goru, and Parh formations in the subcrop (Fig. 1a-b)[19], extending up to the Indus shelf in Pakistan[26]. The entirely siliciclastic Pariwar Formation overlies the Bhadesar Formation unconformably. The upper contact of the Pariwar Formation with the overlying Habur Formation is marked by an unconformity[19]. The upper contact of the Habur Formation with the Paleocene Sanu Formation is a disconformity. The Pariwar Formation primarily represents deltaic to shallow marine deposition, whereas the Habur Formation shows nearshore characteristics[19,22]. Jaisalmer Basin is a proven gas-producing field, where both the Pariwar and Goru formations are important reservoirs[22,25].

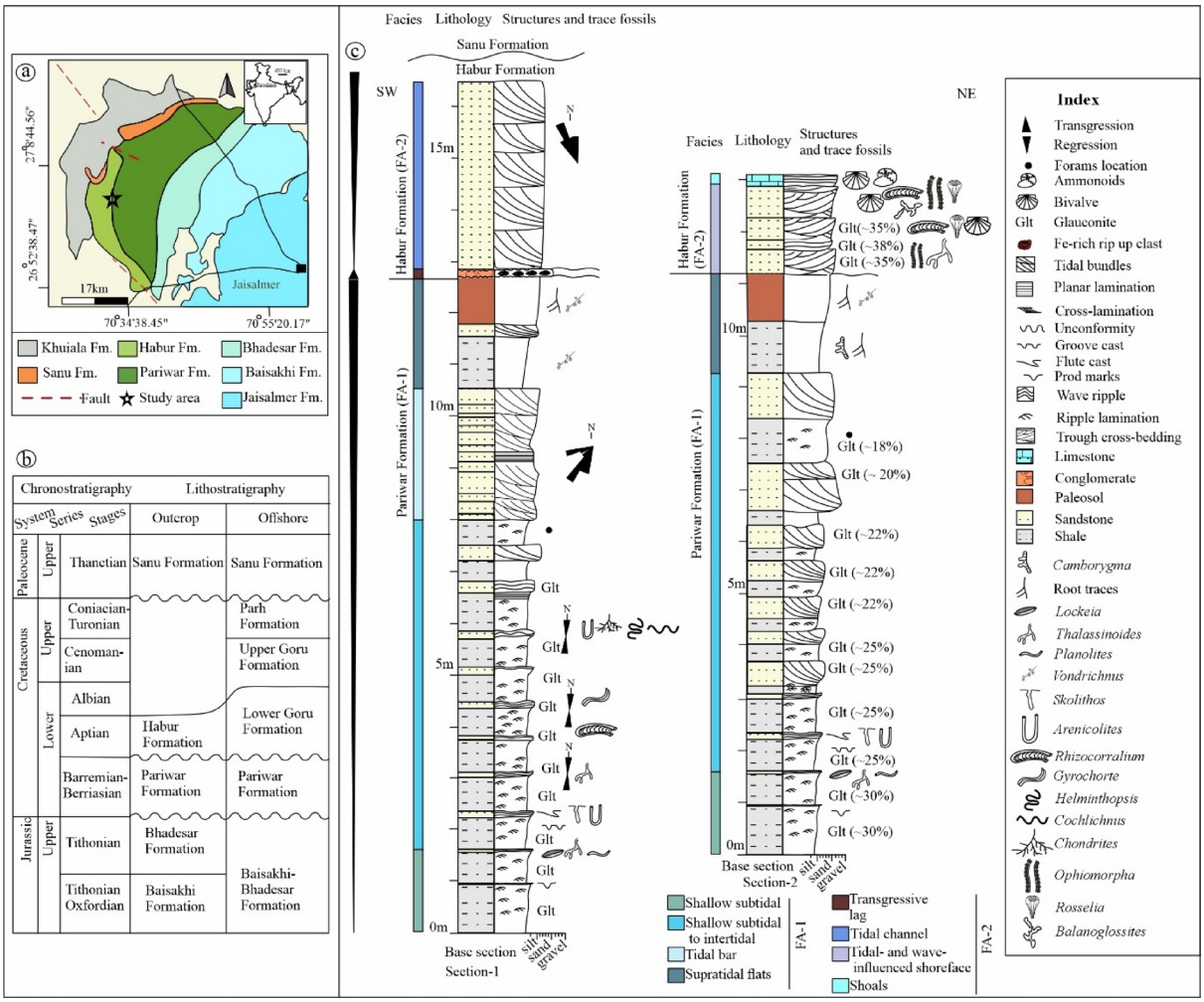

Fig. 1. Geological map of Jaisalmer basin (map modified after[19] showing outcrop of Cretaceous sediments of the basin **(a)**, relevant stratigraphic details **(b)**, detailed lithologs showing the glauconite-bearing upper parts of the Pariwar and Habur formations **(c)**. Note: The glauconite percentage represents volumetric proportion. The sedimentary structures, ichnofossil assemblages, location of microfossils, and depositional conditions are also indicated.

This study focuses on Early Cretaceous outcrops, consisting of the upper part of the Pariwar Formation and the lower part of the Habur Formation. The presence of plant fossils and rarely preserved foraminifera indicates a Neocomian age for the Pariwar Formation[27–30]. Based on ammonite biostratigraphy, the age of the Habur Formation is constrained as Aptian[19,31].

Results

Sedimentary facies analysis

The detailed facies description, including lithology (Fig. 1c), sedimentary structures (Fig. 2), ichnology (Figs. 3 and 4), and micropaleontological data, is presented below (see also Supplementary Table 1). The facies

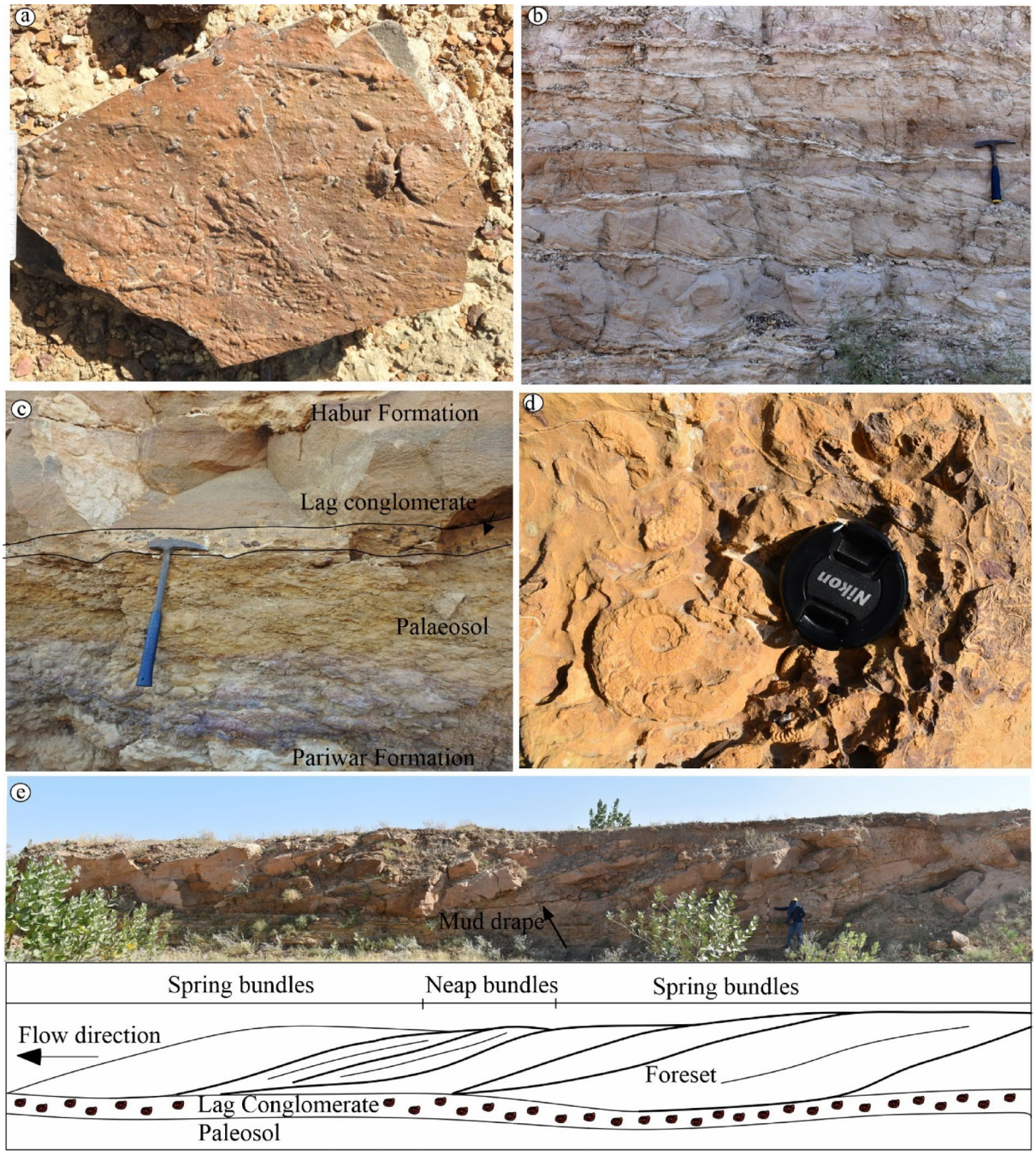

Fig. 2. Field photograph showing a sandstone slab of Pariwar Formation containing tool marks **(a)**, tidal bundles along with reactivation surfaces **(b)**, contact between Pariwar and Habur formations **(c)**, ammonite and bivalves in the limestone **(d)**, Outcrop showing a large-scale sigmoidal cross bedding showing tidal bundles above and sketch of the same feature below **(e)**.

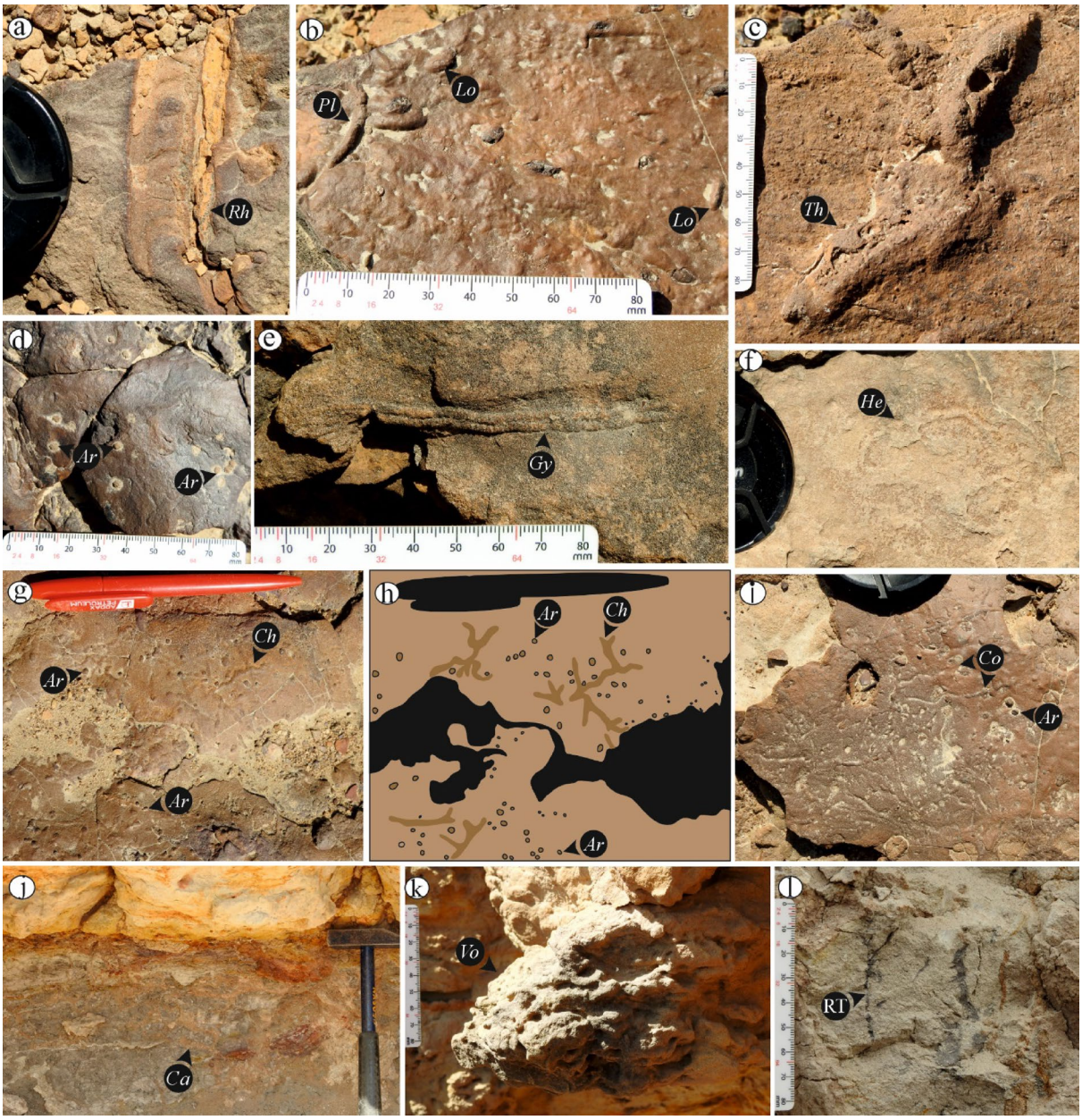

Fig. 3. Ichnocoenoses of the Pariwar Formation. Field photographs and a sketch of marine trace fossils **(a-i)**. Field photographs of continental trace fossils **(j-l)**. *Rh*: *Rhizocorralium*; *Pl*: *Planolites*; *Lo*: *Lockeia*; *Th*: *Thalassinoides*; *Ar*: *Arenocolites*; *Gy*: *Gyrochorte*; *He*: *Helminthopsis*; *Ch*: *Chondrites*; *Co*: *Cochlichnus*; *Ca*: *Camborygma*; *Vo*: *Vondrichnus*; RT: Root Trace.

constituting the Pariwar and Habur formations are grouped into two facies associations, referred to as Facies Association-1 (FA-1) and Facies Association-2 (FA-2), respectively.

Facies Association-1 (FA-1)

Shale

Occurring at the base of the measured section, the 1.5–1.7 m thick shale facies comprises alternations between shale and siltstone, with occasional very fine-grained sandstone interbeds. The thickness of shale and siltstone alternation ranges from 0.5 to 1.1 m, while the thin sheet-like sandstone beds are < 2 cm thick. The shale contains 30% green clays. The siltstone beds are mainly ripple laminated, while fine sandstone beds exhibit wavy laminae at the top. Prod marks and trace fossils may be found occasionally at the base of the sandstone beds. The main ichnotaxa in the sandstone bed include *Planolites*, *Lockeia*, and *Thalassinoides*. The small-sized (< 1 cm), convex, almond-shaped *Lockeia*[35] occur as positive hyporeliefs. The horizontally-oriented, branched, cylindrical burrows are attributed to *Thalassinoides*[36]. The simple, straight, unlined, unbranched, cylindrical to

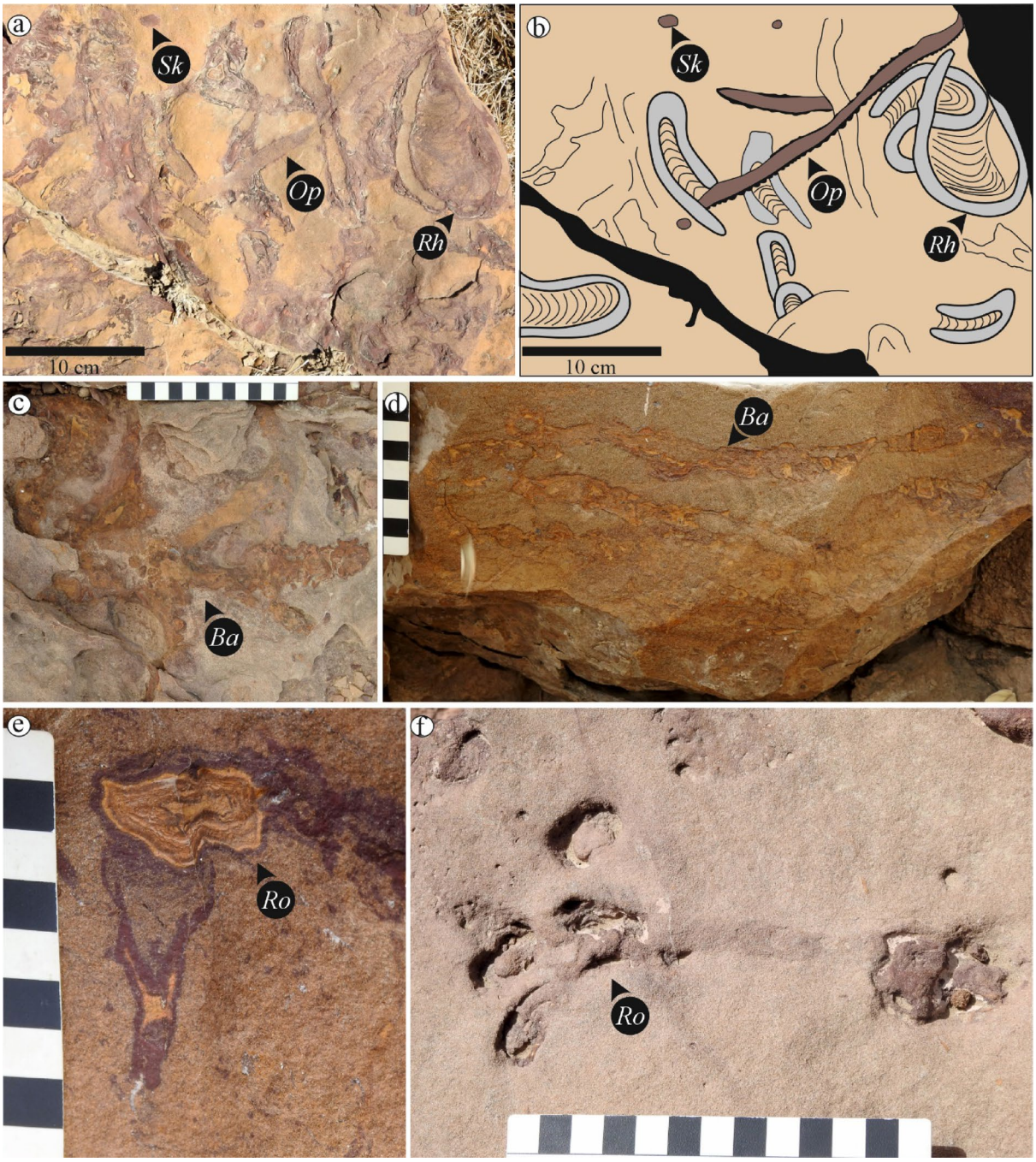

Fig. 4. Ichnocoenoses of the Habur Formation. Complex ichnofabric of *Skolithos*, *Ophiomorpha*, and *Rhizocorralium* representing the softground colonisation **(a-b**, **e-f)**. Firmground colonisation represented by *Balanoglossites***(c-d)**. *Sk*: *Skolithos*; *Op*: *Ophiomorpha*; *Rh*: *Rhizocorralium*; *Ro*: *Rosselia*; *Ba*: *Balanoglossites*.

subcylindrical burrows are characterised as *Planolites*[37]. The shale is completely devoid of benthic and planktic foraminifera.

Heterolithics

This non-repetitive facies overlies the shale facies, consisting of alternations between shale and fine sandstone. The thickness of the facies varies from 6.5 m to 8 m, with shale varying from 60 cm to 80 cm, and sandstone bed thickness exceeding 5 cm. The arkosic sandstone is fine-grained and moderately sorted. Green clay comprises up to 25% of sandstone and shale. The abundance of green clay decreases, and the sand content gradually increases toward the top of the facies. The shale is planar laminated, whereas tabular-shaped sandstone beds show a transition from planar laminae to cross-stratification, and are topped by wave ripples. The wave ripple crests trend in a north-south direction. The soles of the sandstone bed exhibit sole marks, including groove and

flute casts (Fig. 2a). Trace fossils occur as positive hyporelief in the sandstone beds (Fig. 3a-i; BI 3–5), while the shale beds are devoid of ichnofossils. The observed ichnotaxa can be arranged in decreasing order of abundance as: *Arenicolites*, *Skolithos*, *Rhizocorallium*, *Gyrochorte*, *Helminthopsis*, *Chondrites*, and *Cochlichnus*. The straight, vertical, cylindrical burrows, appearing as small circular openings on bedding planes, are *Skolithos*[38]. The equal-sized, paired occurrences of similar circular impressions on the bedding plane represent *Arenicolites*[39], which are characterized by U-shaped burrows in a vertical section. The horizontally-oriented, U-shaped burrows with spreite represent *Rhizocorallium* (*R. commune*)[40,41]. *Gyrochorte*[42] is identified as horizontal, segmented, bilaterally symmetrical burrows that are cylindrical to slightly flattened, often with raised margins. The irregular, winding, to meandering, unbranched horizontal trails represent *Helminthopsis*[43]. Irregularly branching, horizontal tunnels are characteristics of *Chondrites*[44]. The sinuous, meandering horizontal trails resembling a sine curve are identified as *Cochlichnus*[45]. The topmost shale is devoid of calcareous planktic and benthic foraminifera, but contains agglutinated foraminifera (Fig. 2). The foraminiferal assemblage consists predominantly of five genera: *Bathysiphon*, *Ammobaculites*, *Ammotium*, *Haplophragmoides*, and *Trochammina*. These taxa are moderately preserved, with specimens often displaying intact wall structures and minimal fragmentation. Plate 1 illustrates representative specimens from each genus identified in these shale intervals, providing visual confirmation of the taxonomic identifications.

Cross-bedded sandstone

This cross-bedded sandstone is up to 2.5 m thick. The sandstone is mainly white to buff-coloured, medium- to coarse-grained, and unbioturbated, overlying the heterolithics facies. The sandstone shows unidirectional cross-stratification (Fig. 2b). The cross-beds are organized into distinct packages, separated by erosional surfaces. Within the packages, mud drapes are present within the foresets. The thickness of foresets and mud drapes in the cross-bedded sandstone varies, from thin foresets with abundant mud drapes to thick foresets with minimal mud drapes. The sandstones are mainly arkosic arenite, composed of subrounded quartz and subangular feldspar, cemented by iron oxide.

Shale with root traces

Overlying the cross-bedded sandstone, it consists of shale and sandstone. The ~ 1 m thick shale occurs at the base, containing black-coloured root traces, brown-coloured termite tunnels, and sub-vertical to sub-horizontal shafts of *Camborygma*[46] (BI 2–3) (Fig. 3j-l). A ~ 1 m thick medium- to coarse-grained, brown sandstone overlying the shale exhibits a mottled appearance (Fig. 2c), with well-preserved root traces and termite traces such as poly-chambered, diffuse nests of *Vondrichnus*[47] (BI 2–3) (Fig. 3k-l).

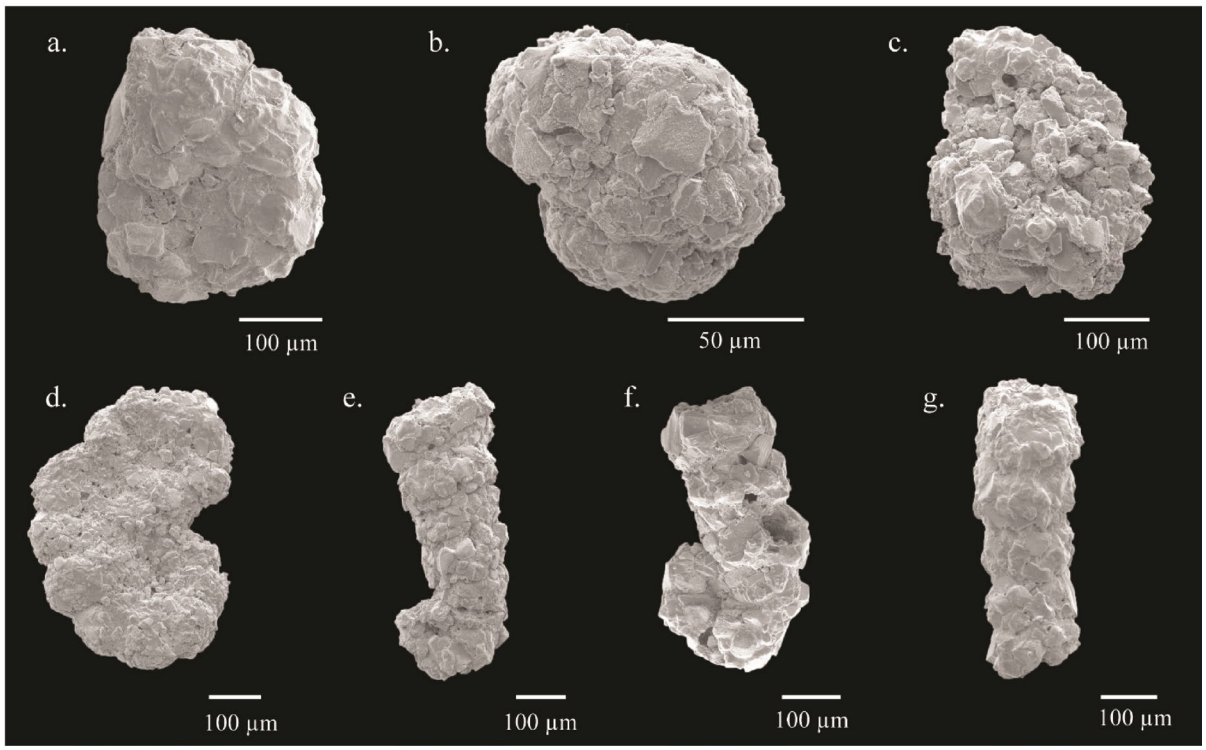

Plate 1. SEM images of an agglutinated foraminiferal assemblage in the shale of heterolithics facies (Pariwar Formation). *Haplophragmoides***(a)**, *Trochammina***(b-c)**, *Ammotium***(d)**, *Ammobaculites***(e-f)**, *Bathysiphon***(g)**.

Interpretations

Shale facies, with minor sandstone beds, represent a low-energy depositional setting that is occasionally affected by high-energy events, resulting in the deposition of sandstone beds. The sharp bases of the sandstone beds, overall grading, and wave-rippled tops indicate possible products of storm deposits[48,49]. The shale facies represent shallow subtidal deposition, and the prevalence of shallow-tier ichnogenera, *Planolites*, *Thalassinoides*, and *Lockeia* at the sand-mud interface suggests episodic stabilization after storm events, and supports subtidal conditions[50].

The overlying heterolithics facies shows a coarsening-upward trend. Paucity of coarse-grained sandstone and absence of fluvial deposits indicate the deposition of sediments away from the river mouth. The sandstones with wave ripples and sole marks represent relatively high-energy events in an overall quiet depositional setting[49]. The vertical burrows (*Arenicolites*, *Skolithos*) in sandstone reflect an association with occasional high-energy conditions[51]. The presence of minor *Chondrites*, *Cochlichnus*, and *Helminthopsis* supports an oxygen-depletion condition between the high-energy events. The consistently small size (< 1 cm diameter) of trace fossils throughout the facies suggests possible environmental stress, including low oxygenation and limited nutrient availability. The Pariwar Formation is a mix of *Skolithos*, distal *Cruziana*, and *Termitichnus* ichnofacies, respectively. The ichnofacies analysis points towards frequent transitions between oxygen-rich and oxygen-depleted environments, where *Skolithos* Ichnofacies represents the former, and distal *Cruziana* Ichnofacies represents the latter. The agglutinated foraminiferal assemblages (*Ammobaculites*, *Ammotium*, *Haplophragmoides*, and *Trochammina)* are typical of shallow marine environments[52–55]. The absence of calcareous foraminifera across the succession corroborates fluctuating salinity, high terrigenous input, and restricted circulation, possibly leading to oxygen stress[56]. The foraminifera taxa *Bathysiphon*, commonly associated with deep-sea settings, have also been documented in low-oxygen, restricted coastal and marginal marine environments[57,58]. Its occurrence in the studied interval likely reflects bottom-water oxygen depletion near the sediment–water interface. Trace fossils and agglutinated foraminiferal assemblages indicate a low-oxygenated, shallow subtidal to lower intertidal deposit, occasionally affected by storm events[50].

The cross-bedded sandstone, overlying sandstone-shale alternations, is formed by the migration of sand waves. Mud drapes within the foresets indicate slack-water deposits related to tidal actions. Thick foresets with fewer mud drapes form during spring tide, while thin foresets with more mud drapes form during neap tide. Foresets with mud drapes reflect water depth, hydrodynamic process, and flow strength during the spring-neap tidal cycle, referred to as the tidal bundle[59–61]. The erosional surface that truncates the top of foresets and separates individual cross-beds suggests a reactivation surface[62]. Overall, the facies is dominated by tidal bundles, indicating a tidal bar[63] with southwest-directed dominant total currents (Fig. 1c). The overlying shale with root traces represents pedogenesis, identified as a paleosol. The ichnogenus *Camborygma* in grey shale is an impression of dominichnial behaviour of the freshwater crayfish, indicating that they thrived near the paleowater table[46–65]. The development of paleosol with prominent root and termite traces (*Vondrichnus*) indicates prolonged subaerial exposure in a supratidal environment[66,67]. The subaerial unconformity, identified by paleosol horizon (Fig. 2c)[68], lies at the top of the Pariwar Formation.

Facies Association-2 (FA-2)

Conglomerate

A 10 cm thick, brownish grey, unbioturbated, tabular-shaped, matrix-supported conglomerate bed sharply overlies the paleosol of the Pariwar Formation. The conglomerate is thin but laterally extensive, consisting primarily of granules, the composition of which matches the paleosol (Fig. 2c). The granules are cemented by iron oxides and are angular to subangular.

Sigmoidal cross-stratified sandstone

The facies is up to 3.5 m thick, overlying the conglomeratic horizon, consisting of sigmoidal cross-stratified sandstone. The sandstone is pink-coloured, coarse-grained, unbioturbated, and displays a rhythmic pattern of cross-beds from convex to concave upward. The thickness of high-angle foreset laminae and mud drapes varies laterally. The cross-beds provide a north-westerly current direction (Fig. 2e). The bottom set of the sigmoidal cross-bed truncates against the underlying conglomerate (Fig. 2e). Petrographic observation reveals coarse-grained, quartz arenite with subangular to subrounded quartz, feldspar (< 5%), cemented by carbonates.

Trough cross-stratified sandstone

It consists of trough cross-bedded, green clay-bearing sandstone and brown coloured sandstone, varying in thickness from 0.2 m to 1.5 m. The green-clay-bearing sandstone at the basal part of the facies is up to 1 m thick. Green clays make up around 30 to 40% of the sandy grains. Green sandstone grades upward into 50 cm-thick brown sandstone containing variable quartz, minor feldspar, and bioclasts, cemented by iron oxide. These beds show trough cross-stratification internally. Wave ripples may occur on top of the sandstone beds occasionally (Fig. 1c). The sandstone beds contain a trace fossil assemblage comprising both softground and firmground ichnotaxa. The softground ichnocoenosis includes *Rhizocorallium*[40], *Ophiomorpha*[69], and *Rosselia*[70], while the firmground assemblage includes the monospecific occurrence of *Balanoglossites*[71]. *Ophiomorpha* exhibits a complex system of horizontal to sub-horizontal boxwork burrows, with walls distinctly lined by agglutinated pellets (Fig. 4a-b). *Rosselia* shows vertical, conical to funnel-shaped burrow architecture, marked by concentric laminae surrounding a central, cylindrical, pencil-thick shaft (Fig. 4e, f). *Balanoglossites* consists of Y- to U-shaped subvertical burrows with non-uniform diameters, scratch marks on walls, and bulbous lateral branches. These burrows lack spreite and are passively filled (Fig. 4c, d).

Limestone

It overlies cross-bedded sandstone sharply and is up to 60 cm thick. It displays large-scale, low-angle trough cross-stratification. The limestone bed contains variable concentrations of clastic grains along with bioclasts like bivalves and ammonites, identified as coquinoid limestone or grainstone (Fig. 2d). The content of carbonate particles is ~ 70%.

Interpretations

The paleosol horizon at the top of the Pariwar Formation marks an unconformity. Immediately overlying the paleosol horizon, developed atop the underlying Pariwar Formation, the conglomerate indicates transgressive lag. Sigmoidal cross-stratified sandstone beds overlying the lag deposit are products of a periodic cycle of spring-neap-spring tides (Fig. 2e). Overall, the facies indicate tidal channel deposits. The trough cross-stratified sandstone facies overlying the paleosol in Sect. "Geological background" indicates migration of the sand bar due to tidal currents. Further, wave ripples on top of the bed reflect the influence of wave action in a shallow marine setting. The ichnogenera *Rhizocorallium*, *Ophiomorpha*, and *Rosselia* comprise *Cruziana* Ichnofacies, manifesting softground colonization that reflects fluctuating energy conditions. *Ophiomorpha*, in particular, indicates high-energy, sandy looseground substrates[72,73]. Monospecific presence of *Balanoglossites*, a characteristic firmground ichnotaxon, in trough-cross-stratified sandstone facies demarcates *Glossifungites* Ichnofacies, suggesting periods of non-deposition or erosion, leading to firmer substrate conditions. These firmgrounds could represent erosion surfaces or discontinuities within an otherwise prograding sequence[65,74]. This erosional exhumation can be a result of allogenic or autogenic sedimentary processes, usually related to allostratigraphic surfaces such as a co-planar surface[50]. Overall, the trough-cross-stratified sandstone facies represent a tidal- and wave-influenced shoreface environment[75]. The occurrence of limestone overlying trough-cross-stratified sandstone beds indicates nearshore deposition influenced by strong oscillatory currents. The presence of bioclasts such as ammonites and bivalve shells, along with pebbly quartz, indicates bioclast-quartz shoals[76]. The admixture of siliciclastic and carbonate components represents possible depositional mixing[77,78] due to the simultaneous transportation of siliciclastic materials on carbonate shoals.

Mode of occurrence of green clay

The green clays occur within shales and sandstones (FA-1) in the Pariwar Formation at depths ranging from 2.8 m to 7 m from the base of the measured section (Fig. 1c). It occurs exclusively as altered forms of fecal pellets, which are spherical (avg. diameter ~ 150 µm; Fig. 5a) to elliptical (avg. dimension of long axes 150–200 µm; Fig. 5b). Green clays in the Habur Formation (FA-2) occur in two distinct forms: altered forms of fecal pellets (Fig. 5c) and infillings within bioclasts, including foraminifera (Fig. 5d). Green pellets and infillings occur mostly as entire forms, and are rarely found broken. In both formations, green clay exhibits olive green colour under plane-polarised light (Fig. 5a-c) and higher order interference colour under crossed-polars, with pinpoint extinction (Fig. 5d). The variable size and shape and moderate to poor sorting of green clays suggest an authigenic origin[1,4]. Additionally, green clay infilling intact bioclasts corroborates an authigenic condition.

The micro-texture of green clay in Pariwar Formation resembles rose-petal structures (Fig. 5e). In contrast, green clay in Habur Formation reflects lamellar micro-texture (Fig. 5f). The X-ray mapping of green clay infillings reveals the enrichment of Al, Fe, K, and Si, while the bioclast tests are outlined by Ca enrichment (Fig. 5g-l).

Mineralogy

X-ray diffraction pattern of the oriented, smear-mounted clay separates exhibits asymmetric reflections at 14.99Å, 10.08Å, 7.15Å, 5.0Å, 4.2Å, 3.5Å, and 3.3Å (Fig. 6a-b). The peaks at 10.1Å, 5.0Å, and 3.3Å remain unaffected by air-drying, glycolation, and heating. The 7Å and 3.5Å peaks are unaffected after air-drying, but peak intensity increases after glycolation, and completely disappear after heating (Fig. 6a-b). The 14.99Å peak shifts to 17.0Å after glycolation and collapses to 10.08Å upon heating. The basal peaks of 4.2Å, 2.6Å remain unaffected after air-drying and glycolation, but shift to 2.7Å, 2.5Å after heating.

The strong reflections of 10.1Å (001), 5.0Å (002), and 3.33Å (003) are characteristics of glauconite. The basal 001 reflection, along with d-spacing and intensity ratios of 001 and 002 planes, confirms the presence of glauconite[1,4,79,80]. The subdued intensity 002 reflection indicates high octahedral iron[4,11,79,80]. The intensity changes of 001 reflection after heating treatment indicate smectite interstratification[5,80–82]. 14.99Å peak, which shifts to 17.0Å after glycolation, indicates a swelling clay. The collapsing of the same peak at 10.08Å after heating confirms montmorillonite[79]. 7Å (001) and 3.5Å (002) peaks, which disappear completely after heating, indicate kaolinite[79]. Strong diffraction peaks at 4.19Å (101), 2.68Å (301), 2.45Å (400), and 1.71Å (212) are of goethite. The shift of these peaks to 2.7Å (104), 2.52Å (110), and 1.69Å (116), along with dominant 104 planes after heating at 400 °C, indicates hematite formed by the alteration of goethite (Fig. 6a-b). The highly intense peaks of 3.34Å ($10\bar{1}$) and 3.24Å (200) indicate quartz and feldspar, respectively.

Mineral chemistry

The chemical composition of glauconite in the Pariwar and Habur formations varies significantly (Supplementary Table 2). The average K_2O content in glauconite pellets from the Pariwar Formation is 6.6 wt%, while the same in the Habur Formation is 7.2 wt%. The average K_2O content of clay infillings in the Habur Formation is 8.1wt%. The average Al_2O_3 content of glauconite pellets is 15wt% and 13wt%, in Pariwar and Habur formations, respectively. The average Al_2O_3 content of clay infillings in the Habur Formation is 9.8 wt%. The average TFe_2O_3 content of glauconite pellets in the Pariwar Formation is 19.4 wt%, and it is 20.1wt% in the Habur Formation. TFe_2O_3 content of glauconite infillings in the Habur Formation exceeds 22 wt%. The average SiO_2 content of

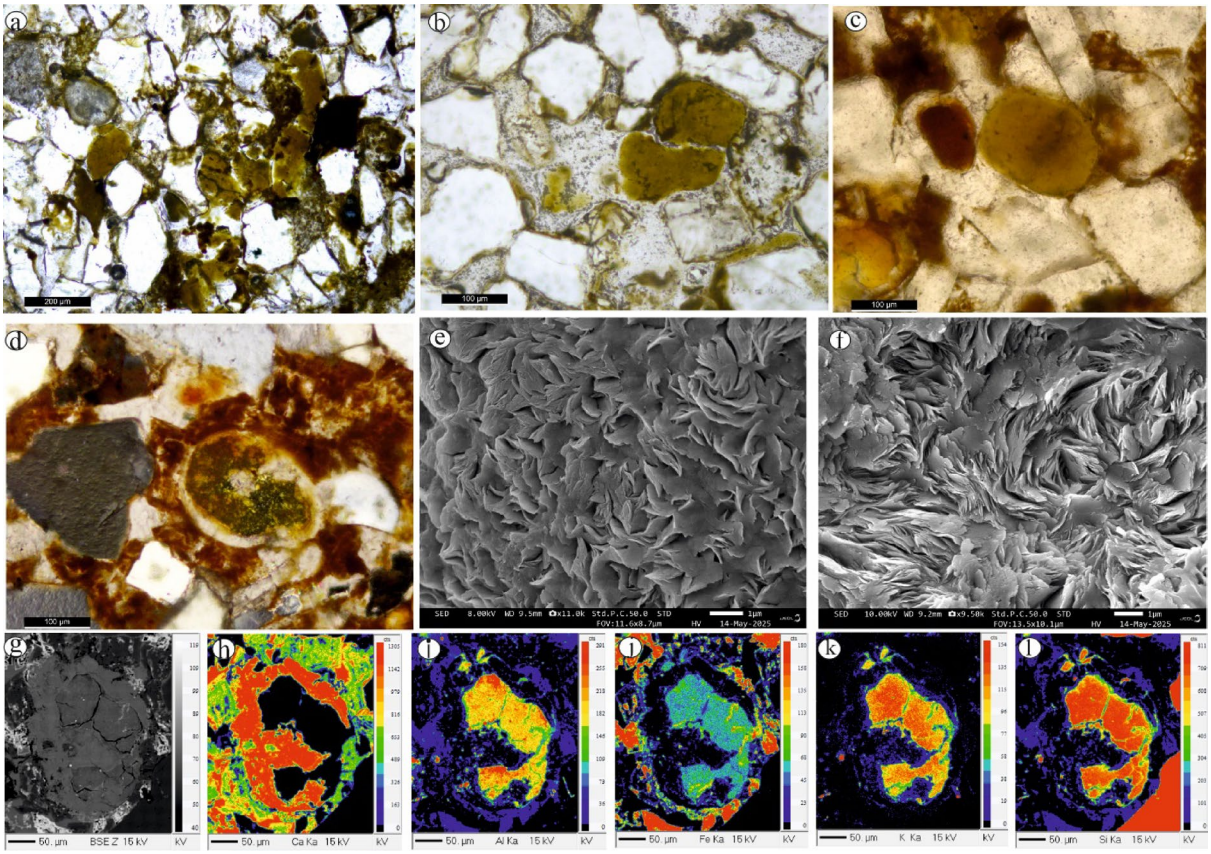

Fig. 5. Photomicrographs under transmitted light showing glauconite pellets in the Pariwar Formation **(a, b)**. Glauconite pellets **(c)** and infillings **(d)** in the Habur Formation **(c, d)**. SEM images showing the rosette texture **(e)** in the Pariwar Formation and lamellar texture in the Habur Formation **(f)**. X-Ray mapping showing compositional variation **(g-l)**. Ca-enrichment indicates part indicates bioclast test **(h)**, while simultaneous enrichment in Al, Fe, K, and Si indicates glauconite infilling within the chambers **(i-l)**.

glauconite in the Pariwar and Habur formations is ~ 51.0 wt%. The average MgO content of glauconite in the Pariwar and Habur formations is ~ 4.2wt%.

Major oxides of glauconites are normalized on an anhydrous background to 100wt% for bi-variant plots. The average SiO_2 content of the glauconite is comparatively lower than published literature[1–3,11,16,82,83]. The K_2O content of glauconite in the Pariwar Formation (av. 6.63wt%) indicates a slightly evolved to evolved composition, whereas the same in the Habur Formation (av. 7.2wt%) reflects an evolved to highly evolved type. The two varieties of glauconites in the Habur Formation are slightly different chemically, as the K_2O content of infillings is higher than that of the pellets. The Al_2O_3 content of the glauconite filling is lower than that of the pellets. The rosette micro-texture of glauconites in the Pariwar Formation corroborates the evolved type glauconite (Fig. 5e). In contrast, the lamellar micro-texture of glauconite in Habur Formation indicates highly evolved nature (Fig. 5f). The TFe_2O_3 vs. K_2O cross-plot of glauconites shows poor correlation ($r^2 = 0.4$ for Pariwar glauconite and $r^2 = 0.6$ for Habur glauconite) (Fig. 6c). The TFe_2O_3 vs. Al_2O_3 cross-plot reveals moderate to good correlation ($r^2 = 0.5$ for Pariwar glauconite and $r^2 = 0.8$ for Habur glauconite; Fig. 6d). The Pariwar and Habur glauconite are compared with published data of Al-glauconite and Paleogene shallow marine glauconite[2,11,18] (Fig. 6d). Both Al_2O_3 and TFe_2O_3 contents are higher in the studied glauconites.

Discussion

Depositional framework

The entirely siliciclastic Pariwar Formation is overall shallowing upward, and it represents landward migration of facies. The FA-1 (Pariwar Formation) (Fig. 1c) represents a depositional environment ranging from shallow subtidal, lower intertidal, tidal bar, to supratidal deposits (Fig. 7). The occurrences of fodinichnial, pascichnial, domichnial, and repichnial moderately-diverse, tiny ichnofossils (< 1 cm) and presence of agglutinated foraminifera *Bathysiphon* indicate oxygen-depleted seawater. Occasional storms possibly disrupt the stratification in the seawater column for a brief period. Further, the oxygen-depleted condition is necessary for glauconite formation[84–88]. The glauconite content in sediments decreases from shallow subtidal to lower intertidal facies and disappears in supratidal facies. The top of the paleosol horizon represents a subaerial unconformity that marks the upper boundary of the Pariwar Formation (Fig. 1c). The lag conglomerate separates the erosional contact between Pariwar and Habur formations, and is a product of reworking during the transgression. The

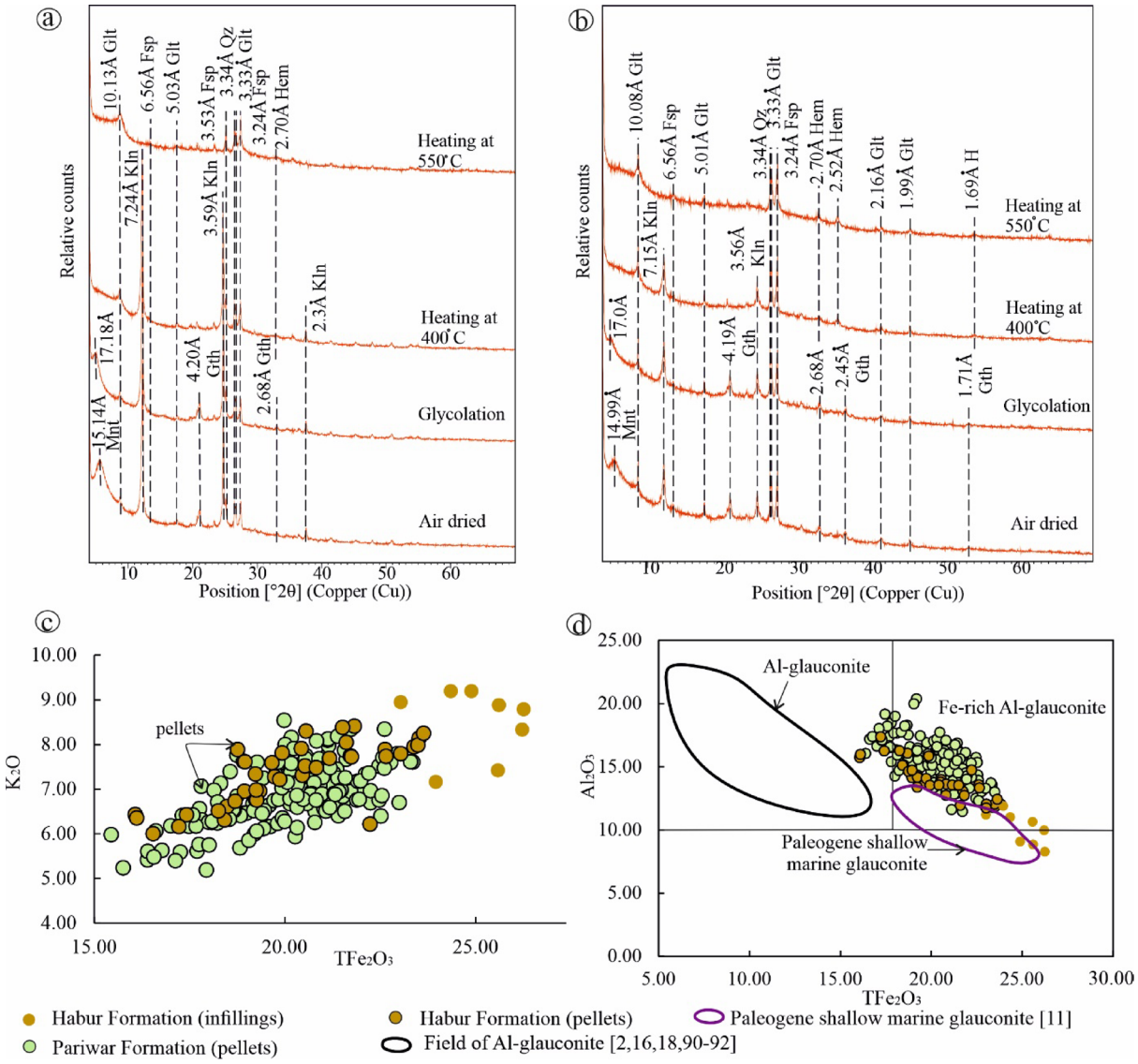

Fig. 6. X-ray diffractogram of the clay-separated samples of Pariwar Formation **(a)** and Habur Formation **(b)**. Note: Qz-Quartz, Fsp-Feldspar, Glt-Glauconite, Gth-Goethite, Hem-Hematite, Kln-Kaolinite, Mnt-Montmorillonite. Bivariant plot of glauconites: Fe_2O_3 vs. K_2O cross-plot **(c)**, Fe_2O_3 vs. Al_2O_3 cross-plot **(d)**. The Al-glauconite has been defined based on published data[18]. The Al-rich glauconites from Precambrian, Paleozoic successions[2,16,18,89,90] and Cretaceous deposits form the cluster at the upper left corner[91]. Paleogene shallow marine glauconite forms a separate cluster[11]. Fe-rich Al-glauconite is demarcated for the first time.

detailed facies analysis and trace fossils of FA-2 (Habur Formation) indicate depositional settings from tidal channel, tidal- and wave-influenced shoreface, to carbonate shoals. In the Habur Formation, glauconite occurs in tidal- and wave-influenced shoreface settings.

Unique compositional characteristics of Cretaceous glauconite in Jaisalmer basin

The Al-glauconite in the Cretaceous Jaisalmer Basin is unique because of its high TFe_2O_3 content. Pariwar and Habur glauconites exhibit a reduced 002 peak in the XRD pattern, indicating high octahedral Fe (Fig. 6a-b). Precambrian and Paleozoic glauconites generally contain high Al_2O_3 and low TFe_2O_3 (< 20 wt%), whereas Mesozoic and Cenozoic glauconites typically contain lower Al_2O_3 (< 15 wt%) and higher TFe_2O_3 (> 20 wt%) contents [2, Fig. 6d]. Al-glauconite is characterized by > 10 wt% Al_2O_3 and < 18 wt% TFe_2O_3, commonly associated with Precambrian and Cambrian, and rarely in Cretaceous sediments (Fig. 6d)[2,16,18,89–91]. Compositionally, Habur and Pariwar Al-glauconites are close to shallow marine Paleogene glauconites because of the high TFe_2O_3 content (Fig. 6d)[11] (Supplementary Table 3). However, more than 50% of Pariwar and Habur Al-glauconites contain Al_2O_3 > 15 wt%, in which TFe_2O_3 exceeds 18 wt%, and therefore, these glauconites form a separate cluster (Fig. 6d). Therefore, based on the compositional characteristics, Pariwar and Habur glauconites have been considered for the first time as Fe-rich Al-glauconite (Fig. 6d).

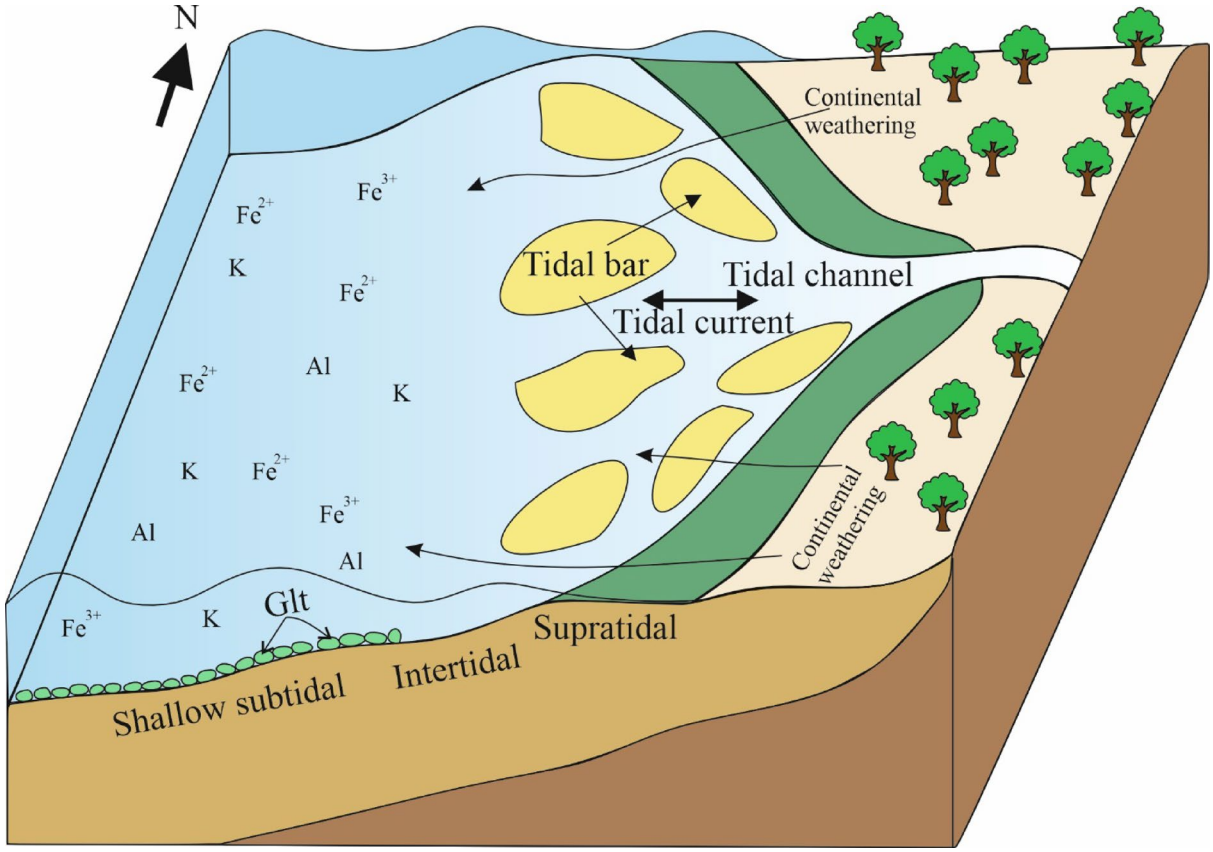

Fig. 7. Depositional model of glauconite formation in marginal marine settings (Glt-Glauconite).

Origin of glauconite

Glauconite formation is explained by three theories: layer lattice, verdissement, or pseudomorphic replacement[1,2,92,93]. Layer lattice theory involves the fixation of Fe^{2+} with K^+ within the degraded 2:1 phyllosilicate structure[1,92]. Verdissement theory[1,2,93] explains the neoformation of glauconitic smectite in porous substrates and its subsequent evolution to glauconite[93]. Pseudomorphic replacement theory involves the dissolution and replacement of the potassium-rich substrate, such as feldspar[1,2]. However, conventional theories do not explain the high contents of Al_2O_3 and TFe_2O_3 in Habur and Pariwar glauconites. Factors such as redox state, substrate composition, elemental sequestration, and micro-environments affect glauconite composition[2–4,11,16,17,82,83,94]. Generally, shallow marine glauconite is enriched in Al due to input from continental weathering, causing high Al flux in seawater, while deep marine glauconite contains high Fe[12,17]. The high Fe content of Fe-rich Al-glauconite may be linked to different mechanisms such as diagenesis, thermal maturity, Al-Fe-rich substrate, and elemental influx due to continental weathering. However, the maturity of organic matter in the studied Cretaceous sediments remains low[25]. Further, several studies indicate that diagenesis leads to the depletion of K and Fe[95–98]. The high content of Al_2O_3 in Parwiar and Habur glauconites is possibly inherited from aluminous substrates such as kaolinite (Equation-i)[12,99]. Fe enrichment in shallow marine conditions is possible through riverine inputs, primarily in the form of iron hydroxide/goethite[12,17]. In such a condition, microbial Fe(III) reduction supplies Fe^{2+} into the environment[17]. Smectite interstratification observed in XRD (Fig. 6a-b) suggests that glauconite might have formed after the smectite precursor. Generally, Fe-smectite substrate dominates in deeper marine settings, while Fe-Al smectite occurs in shallow marine conditions[17]. Subsequently, kaolinite and Fe-Al-smectite react in the presence of excess Fe to form a glauconite pellet (Equation-ii). As a result, authigenesis of Fe-rich Al-glauconite can be expressed by a combination of the following reactions, proposed in a few studies[11,99–101].

$$\begin{aligned}\text{Kaolinite} + \text{Montmorillonite} \rightarrow \text{Mixed layer mineral} + \text{Amorphous silica} + K^+ \\ + \text{Iron hydroxide/goethite} \rightarrow \text{illite-smectite mixed layer mineral} \\ + HCO^-{}_3 \rightarrow \text{Fe-rich Al-glauconite} + \text{Smectite} + CO_2 + H_2O\end{aligned} \quad (1)$$

$$\begin{aligned}\text{Al-Fe-smectite} + \text{Kaolinite} + K^+ \rightarrow \text{Mixed layer mineral} + HCO^-{}_3 \rightarrow \text{Fe-rich Al-glauconite} \\ + \text{Smectite} + CO_2 + H_2O\end{aligned} \quad (2)$$

High alumina glauconite typically forms within an Al-rich substrate, including kaolinite and feldspar. Most of these glauconites are found in shallow marine environments. A few studies report a high (>15wt%) TFe_2O_3 content in Al-glauconites in ~10% of total glauconite data (Supplementary Table 3). In contrast, the present glauconite data indicate an advanced stage of alteration of high-alumina substrates.

Implications of glauconite formation in shallow marine conditions

The characteristics of Early Cretaceous Habur and Pariwar glauconites are different compared with their ancient counterparts[2,4,11,87–89,102–104]. Glauconite composition reflects unusual seawater chemistry, abnormal elemental influx due to continental weathering, and availability of Al-Fe-rich substrate. Several studies indicate that glauconite formation requires suboxic conditions[3,84–88]. The dominance of deposit and detritus feeding traces, moderate ichnodiversity, along with their stunted size (< 1 cm diameter), indicates a dysaerobic/dysoxic condition[50,105]. The mix of *Skolithos* and distal *Cruziana* ichnofacies also signals a shallowing-deepening trend and post-depositional dysoxia. The occurrence of trace fossils on bedding planes of sandstones and their absence in shale beds corroborates the oxygen-depleted condition in the substrate, which prevented the organisms from thriving within the sediment; instead, they survived at the sediment-water interface. The presence of agglutinated foraminiferal taxa, particularly *Bathysiphon*, supports oxygen-depleted conditions in a marginal marine setting[57,58]. The development of oxygen-depleted conditions in marginal marine settings indicates landward expansion of the OMZ (Oxygen Minimum Zone) onto the shallow shelf during the Cretaceous. Oxygen depletion in a marginal marine setting may be caused by several factors, including coastal hypoxia, stratification in the water column, and the expansion of the oxygen minimum zone during greenhouse conditions[98,106–108]. Early Cretaceous represents a global warming period[109], with an oxygen anoxic event (OAE), which leads to the expansion of OMZ irrespective of local basin geometry[110]. The occurrences of Fe-rich Al-glauconite during this interval further support suboxic conditions in the shallow sea[2,13,14], besides local factors such as hydrothermal alteration and volcanism (Supplementary Table 3). The intense chemical weathering and consequent high influx of K, Al, and Fe in the seawater facilitate glauconite formation[9,111,112]. Thus, the unusual seawater chemistry, enriched in Al, K, and highly reactive Fe^{2+} in suboxic conditions, promotes marginal marine glauconitization in a warm, humid climate.

Conclusions

- The Al-glauconites in Pariwar and Habur formations are compositionally distinct as these contain high TFe_2O_3 (>18wt%), and are considered as Fe-rich Al-glauconite. The X-ray diffraction, K_2O content, and micro-texture indicate evolved to highly evolved glauconite. The glauconite forms within the marginal marine environment from shallow subtidal to tidal- and wave-influenced shoreface settings as fecal pellets and bioclast infillings.
- Trace fossils (< 1 cm diameter) and agglutinated foraminifera (*Bathysiphon)* indicate oxygen-depleted conditions. The low-oxygenated conditions and landward expansion of OMZ during the Early Cretaceous induce glauconitization in marginal marine settings by mobilizing Fe^{2+}.
- Kaolinite and Fe-Al-smectite react in the presence of excess Fe to form compositionally unique Fe-rich Al-glauconite. The distinctive composition of glauconite reflects the unusual composition of Cretaceous seawater and intense chemical weathering during the Cretaceous greenhouse climate.

Samples and methods

Fieldwork was conducted around Habur (27°8'40.20" N, 70°33'4.14" E, to 27°7'47.32" N, 70°32'49.42" E), covering the outcrops of the upper part of the Pariwar and lower part of the Habur formations, and the sections were measured using Jacob's staff and measuring tape. The base of the measured section rests ~40 m above the unconformable contact with the Bhadesear Formation. A detailed lithology was prepared, and samples were collected systematically, marking their positions in the log. 24 thin sections were prepared and examined using a Leica DM 4500P polarizing microscope, and photographs were captured using Leica DFC420 camera attached to the microscope at the Department of Earth Sciences, Indian Institute of Technology (IIT) Bombay. The volumetric percentage of glauconite (Fig. 1c) was determined using the Gazzi–Dickinson point counting method. X-ray diffraction (XRD) analysis was conducted on 10 samples of clay-bearing sandstone and shale. The samples were powdered, and clay fractions (<2 µm grain size) were separated using gravimetric settling and centrifugation. The clay samples were analyzed as oriented smear-mounted preparations under four conditions: air-dried, glycolation (ethylene glycol solvent for 1 h), and after heating at 400 °C, 550 °C. Scanning was performed from 4° to 70° 2θ, with a step size of 0.026° 2θ and a scan speed of 96 s/step, using nickel-filtered copper radiation on an Empyrean X-Ray Diffractometer with a Pixel 3D detector at IIT Bombay. Clay minerals were identified based on basal (hkl) reflections[79] using Panalytical© HighScore™ software. The major oxide analysis and elemental mapping of green clays were performed using a Cameca SX Five Electron Probe Micro Analyzer (EPMA), with an accelerating voltage of 15 kV, specimen current of 40 nA, and a beam diameter of 1 µm (peak: 10–20 s and background counting: 5–10 s) at the Department of Earth Sciences, IIT Bombay. Natural minerals, including albite (for Na Kα), orthoclase (for K Kα), diopside (for Ca Kα, Mg Kα), apatite (for P Kα), and rhodonite (for Mn Kα), as well as synthetic mineral phases including $CaSiO_3$ (for Si Kα), Fe_2O_3 (for Fe Kα), and Al_2O_3 (for Al Kα), were used as standards for the calibration of the major oxide analysis. The individual points show analytical error < 1%. For micro-textural analysis, handpicked green clays were mounted on the stub and examined using a JEOL JSM-IT800 Field Emission Gun Scanning Electron Microscope (FEG-SEM) and Energy Dispersive X-ray Fluorescence (EDXRF) Analysis System, at the Department of Earth Sciences, IIT Bombay.

The trace fossils were identified in situ, photographed systematically, and documented along with the respective lithounits. The ichnological parameters, such as bioturbation index (BI), ichnofabric, and ichnofacies, were recorded using established methods[50,113]. For micropaleontological studies, approximately 20 g of each sample was used. Samples were crushed into pea-sized fragments and treated with a 3% hydrogen peroxide (H_2O_2) solution in labelled glass beakers to oxidize the organic carbon. After soaking for 8–10 h, ultrasonic cleaning was applied for 15–20 s to remove adhering mud particles. Each sample was then carefully washed through a stack of sieves with mesh sizes of 63 µm and 25 µm under low water pressure to separate the foraminiferal specimens. The cleaned residues were left to dry overnight in an oven at 50 °C. Quantitative faunal analysis of agglutinated foraminifera was conducted on representative sample splits (using an Otto microsplitter) containing at least 300 specimens from the 63–500 µm size fraction. All specimens within these splits were hand-picked, taxonomically identified to the genus level, counted, and mounted on micropaleontological slides for permanent archiving. Selected specimens were photographed using a JEOL JSM-IT800 Field Emission Gun Scanning Electron Microscope (FEG-SEM). Species-level diagnosis was not done owing to the moderate to poor preservation. Taxonomic definitions that were adapted from standard literature[32–34].

Data availability

The data generation and analysis during the study are presented in the article and the Supplementary file. All data are available with the corresponding author. For any data availability, corresponding author may be contacted.

Received: 4 August 2025; Accepted: 18 September 2025
Published online: 24 October 2025

References

1. Odin, G. S. & Matter, A. De glauconiarum origine. *Sedimentology* **28**, 611–641 (1981).
2. Banerjee, S. & Bansal, U. Vilas Thorat, A. A review on palaeogeographic implications and Temporal variation in glaucony composition. *J. Palaeogeography*. **5**, 43–71 (2016).
3. Banerjee, S., Chattoraj, S. L., Saraswati, P. K., Dasgupta, S. & Sarkar, U. Substrate control on formation and maturation of glauconites in the middle eocene Harudi Formation, Western Kutch, India. *Mar. Pet. Geol.* **30**, 144–160 (2012).
4. Banerjee, S., Mondal, S., Chakraborty, P. P. & Meena, S. S. Distinctive compositional characteristics and evolutionary trend of precambrian glaucony: example from Bhalukona Formation, Chhattisgarh basin, India. *Precambrian Res.* **271**, 33–48 (2015).
5. Baldermann, A., Warr, L. N., Grathoff, G. H. & Dietzel, M. The rate and mechanism of deep-sea glauconite formation at the Ivory Coast–Ghana marginal ridge. *Clays Clay Miner.* **61** (3), 258–276 (2013).
6. Baldermann, A. et al. Exploring reverse silicate weathering across geological time: a review. *Clay Miner.* **60** (1), 1–27 (2025).
7. Rudmin, M. et al. Roasting-leaching experiments on glauconitic rocks of Bakchar ironstone deposit (Western Siberia) for evaluation their fertilizer potential. *Appl. Clay Sci.* **162**, 121–128 (2018).
8. Bansal, U., Böning, P. & Wilmsen, M. Enhanced chemical weathering of the continents promoted fast late cretaceous nearshore glaucony formation: implications from the Danubian cretaceous Group, Germany. *J. Geol. Soc.* **180** (2), 2022–2098 (2023).
9. Wilmsen, M., Bansal, U., Metzner, N. & Böning, P. Geochemical and depositional environment of an upper cretaceous greensand giant (Münsterland cretaceous Basin, Germany). *Chem. Geol.* **661**, 122–168 (2024).
10. Banerjee, S., Choudhury, T. R., Saraswati, P. K. & Khanolkar, S. The formation of authigenic deposits during paleogene warm Climatic intervals: a review. *J. Palaeogeography*. **9**, 1–27 (2020).
11. Choudhury, T. R., Banerjee, S., Khanolkar, S., Saraswati, P. K. & Meena, S. S. Glauconite authigenesis during the onset of the Paleocene-Eocene thermal maximum: A case study from the Khuiala formation in Jaisalmer Basin, India. *Palaeogeogr., Palaeoclimatol. Palaeoecol.* **571**, 110388 (2021).
12. Baldermann, A. et al. Impact of green clay authigenesis on element sequestration in marine settings. *Nat. Commun.* **13** (1), 1527 (2022).
13. Reeder, S. W., Hitchon, B. & Levinson, A. A. Hydrogeochemistry of the surface waters of the Mackenzie river drainage basin, Canada—I. Factors controlling inorganic composition. *Geochim. Cosmochim. Acta*. **36** (8), 825–865 (1972).
14. El Albani, A., Meunier, A. & Fürsich, F. Unusual occurrence of glauconite in a shallow lagoonal environment (Lower Cretaceous, Northern Aquitaine Basin, SW France). *Terra Nova*. **17** (6), 537–544 (2005).
15. Chafetz, H. S. & Reid, A. Syndepositional shallow-water precipitation of glauconitic minerals. *Sed. Geol.* **136** (1–2), 29–42 (2000).
16. Tang, D. et al. Formation of shallow-water glaucony in weakly oxygenated precambrian ocean: an example from the mesoproterozoic Tieling formation in North China. *Precambrian Res.* **294**, 214–229 (2017).
17. Baldermann, A. et al. The role of Fe on the formation and diagenesis of interstratified glauconite-smectite and illite-smectite: A case study of upper cretaceous shallow-water carbonates. *Chem. Geol.* **453**, 21–34 (2017).
18. Berg-Madsen, V. High-alumina glaucony from the middle cambrian of Öland and Bornholm, Southern Baltoscandia. *J. Sediment. Res.* **53** (3), 875–893 (1983).
19. Singh, N. P. Mesozoic lithostratigraphy of the Jaisalmer basin, Rajasthan. *J. Palaeontol. Soc. India*. **51** (2), 1–25 (2006).
20. Rai, J., Singh, A. & Pandey, D. K. Early to middle Albian age calcareous nannofossils from Pariwar formation of Jaisalmer Basin, Rajasthan, Western India and their significance. *Curr. Sci.* **105**, 1604–1611 (2013).
21. Kumar, R., Aggarwal, N., Das, N., Pandey, B. & Kumar, K. Palaeoenvironmental reconstruction based on palynofacies analysis of the early to middle jurassic of the lathi Formation, Jaisalmer Basin, India. *J. Palaeontol. Soc. India*. **67** (2), 262–273 (2022).
22. Verma, S. K., Chakrabarty, S., Gorai, D. & Microfacies Depositional Environment and Origin of low resistivity sandstone in Lower Cretaceous Pariwar Formation, Jaisalmer Basin, India. *SPG* (2020).
23. Krishna, J. An overview of the mesozoic stratigraphy of Kachchh and Jaisalmer basins. *J. Palaeontol. Soc. India*. **32**, 136–149 (1987).
24. Pandey, D. et al. A review of the Lower-lowermost upper jurassic facies and stratigraphy of the Jaisalmer Basin, Western Rajasthan, India. *Volumina Jurassica*. **10** (1), 61–82 (2012).
25. Pandey, R., Aswal, M. L., Shah, L. & Mahanti, S. A note on sand geometry and Paleo-environmental analysis of lower Goru and Pariwar sands, Jaisalmer Basin, India. *Indian Near Surf. Geophys. Conf. Exhib.* **1**, 1–13 (2019).
26. Dar, Q. et al. Depositional facies and reservoir characteristics of the early cretaceous lower Goru Formation, lower indus basin pakistan: integration of petrographic and gamma-ray log analysis. *Petroleum* **9** (3), 331–341 (2023).
27. Sigal, J., Singh, N. P., Canon, A. & Ernst, M. Sur l age et les affinities Gondwanicnnes de microfaunes (Foraminifercs et ostracodes) malgaches, Indicnncs Ct Chillicnnes Au Sommet du Jurassique et Ala base du Crtacc. *Acad. Sci. Paris*. **271**, 24–27 (1970).
28. Sigal, J. & Singh, N. P. Cretaceous biostratigraphy of Jaisalmer subsurface, Rajasthan. *India VIIIth Colloq. Ind. Micropal Strat* 22–23 (1980).

29. Dasgupta, S. K. Revision of the Mesozoic-Tertiary stratigraphy of the Jaisalmer basin, Rajasthan. *Indian J. Earth Sci.* **2** (1), 77–94 (1975).
30. Das, N., Kumar, R., Pandey, B., Kumar, K. & Bhattacharya, D. Record of plant fossils from freshly discovered succession of the Pariwar Formation, Jaisalmer Basin, Western India. *Hist. Biol.* **33** (12), 3281–3290 (2021).
31. Spath, L. F. Revision of jurassic cephalopods from Kutch. *Palaeontologica Indica New. Series* **2**, I–VI (1933).
32. Loeblich, A. R. Jr & Tappan, H. *Foraminiferal Genera and their Classification* (Springer, 2015).
33. Kaminski, M. A. & Gradstein, F. M. *Atlas of Paleogene cosmopolitan deep-water agglutinated foraminifera*. (2005).
34. Setoyama, E., Kaminski, M. A. & Tyszka, J. Late Cretaceous–Paleogene foraminiferal morphogroups as palaeoenvironmental tracers of the rifted Labrador margin, Northern proto-Atlantic. *Grzybowski Foundation Special Publication*. **22**, 179–220 (2017).
35. James, U. P. Description of new species of fossils and remarks on some others, from the lower and upper silurian rocks of Ohio. *Paleontologist* **3**, 17–24 (1879).
36. Ehrenberg, K. Erg¨ anzende bemerkungen Zu Den Seinerzeit Aus dem Mioz¨ an von Burgschleinitz beschriebenen Gangkernen und Bauten Dekapoder Krebse. *PalZ* **23**, 354–359 (1944).
37. Nicholson, H. A. Contributions to the study of the errant annelides of the older palaeozoic rocks. *Proc. Royal Soc. Lond.* **21**, 288–290 (1873).
38. Haldeman, S. S. A monograph of the Limniades, and other freshwater bivalve shells of the apparently new animals in different classes, and names and characters of the subgenera in paludina and anculosa. *J. Dobson Philadelphia* **3**, 3 (1840).
39. Salter, J. W. On annelide burrows and surface markings from the cambrian rocks of the Longmynd. *Q. J. Geol. Soc.* **13**, 199–207 (1857).
40. Zenker, J. C. *Historisch-topographisches Taschenbuch von Jena und seiner Umgebung. Friedrich Frommann.* (1836).
41. Schmid, E. E. *Der Muschelkalk des östlichen Thüringen. Fromann.* (1876).
42. Heer, O. *Die Urwelt der Schweiz*. (1865).
43. Heer, O. *Flora fossilis Helvetiae*. (1877).
44. Sternberg, K. M. V. Versuch einer geognostisch-botanischen darstellung der flora der Vorwelt, band II, hefte 5 und 6 attempt to a geognostic-botanical representation of the flora of the ancient world. *J. Spurny Prague*. **II** (5/6), 94 (1833).
45. Hitchcock, E. *Ichnology of New England; a report on the sandstone of the Connecticut Valley, especially its footmarks.* 1–220 (1858).
46. Hasiotis, S. T. & Mitchell, C. E. A comparison of crayfish burrow morphologies: triassic and holocene fossil, paleo-and neo-ichnological evidence, and the identification of their burrowing signatures. *Ichnos: Int. J. Plant. Anim.* **2** (4), 291–314 (1993).
47. Duringer, P. et al. New termite trace fossils: Galleries, nests and fungus combs from the Chad basin of Africa (Upper Miocene–Lower Pliocene). *Palaeogeogr., Palaeoclimatol. Palaeoecol.* **251** (3–4), 323–353 (2007).
48. Sarkar, S., Banerjee, S., Chakraborty, S. & Bose, P. K. Shelf storm flow dynamics: insight from the mesoproterozoic Rampur Shale, central India. *Sed. Geol.* **147** (1–2), 89–104 (2002).
49. Poyatos-Moré, M. et al. Sharp-based, mixed carbonate–siliciclastic shallow-marine deposits (upper Miocene, Betic Cordillera, Spain): the record of ancient transgressive shelf ridges? *Sed. Geol.* **429**, 106077 (2022).
50. Buatois, L. A. & Mangano, M. G. *Ichnology: Organism Substrate Interactions in Space and time* (Cambridge University Press, 2011).
51. Knaust, D. *Atlas of Trace Fossils in Well Core: appearance, Taxonomy and Interpretation* (Springer, 2017).
52. Schröder-Adams, C. Estuaries of the past and present: A biofacies perspective. *Sed. Geol.* **190** (1–4), 289–298 (2006).
53. Murray, J. W., Alve, E. & Jones, B. W. A new look at modern agglutinated benthic foraminiferal morphogroups: their value in palaeoecological interpretation. *Palaeogeogr., Palaeoclimatol. Palaeoecol.* **309** (3–4), 229–241 (2011).
54. Sprong, J. et al. Characterization of the latest Danian event by means of benthic foraminiferal assemblages along a depth transect at the Southern Tethyan margin (Nile Basin, Egypt). *Mar. Micropaleontol.* **86**, 15–31 (2012).
55. Haig, D. W. Ammobaculites (Foraminifera): living fossils in Southern Western Australian estuaries. *J. R. Soc. West. Aust.* **103**, 57–77 (2020).
56. Saraswati, P. K. *Foraminiferal micropaleontology for understanding Earth's history* (Elsevier, 2021).
57. Jones, R. W. *Foraminifera and their Applications* (Cambridge University Press, 2013).
58. Anan, H. S. Representatives of some diagnostic agglutinated foraminiferal genera of the subclass monothalamana (Bathysiphon, Orbulinelloides, Repmanina, Miliammina, Agglutinella, Dentostomenia, Ammomassilina, Psammolingulina) in the Tethys. *Geol. Behav. (GBR)*. **5** (2), 53–58 (2021).
59. De Mowbray, T. & Visser, M. J. Reactivation surfaces in subtidal channel deposits, Oosterschelde, Southwest Netherlands. *J. Sediment. Res.* **54** (3), 811–824 (1984).
60. Nio, S. D. & Yang, C. S. Sea-level fluctuations and the geometric variability of tide-dominated sandbodies. *Sed. Geol.* **70**, 161–193 (1991).
61. Choi, K. Morphologic and hydrodynamic controls on the occurrence of tidal bundles in an open-coast macrotidal environment, Northern Gyeonggi Bay, West Coast of Korea. *Sed. Geol.* **339**, 68–82 (2016).
62. Bose, P. K. & Chakraborty, P. P. Marine to fluvial transition: proterozoic upper Rewa sandstone, Maihar, India. *Sed. Geol.* **89**, 285–302 (1994).
63. Olariu, C., Steel, R. J., Dalrymple, R. W. & Gingras, M. K. Tidal dunes versus tidal bars: the sedimentological and architectural characteristics of compound dunes in a tidal seaway, the lower Baronia sandstone (Lower Eocene), ager Basin, Spain. *Sed. Geol.* **279**, 134–155 (2012).
64. Hasiotis, S. T. Continental ichnology: Fundamental processes and controls on trace fossil distribution. In: Miller III, W. (Ed.), *Trace Fossils* 268–284 (2007).
65. Das, M., Dasgupta, S., Singh, S., Klunk, M. A. & D'souza, R. The *Camborygma* ichnofacies in a high-resolution sequence-stratigraphic framework for the eocene palustrine-alluvial depositional interval of the Kutch Basin, India. *J. Palaeo.* **14** (1), 141–156 (2025).
66. Zecchin, M. & Catuneanu, O. High-resolution sequence stratigraphy of clastic shelves I: units and bounding surfaces. *Mar. Pet. Geol.* **39** (1), 1–25 (2013).
67. Srivastava, A., Dasgupta, S. & Singh, S. Lower-order transgressive–regressive cycles within a higher-order transgression at the basin margin: an aberrant intercalation of palaeosol and biostromal ichnofabrics from the early miocene Kutch Basin, India. *J. Palaeogeography*. **13** (4), 906–923 (2024).
68. Alekseeva, T. V., Malyshev, V. V. & Alekseev, A. O. Paleosols as markers of stratigraphic unconformities in the upper Visean rocks of the Mstikhino Section, Kaluga oblast: Geochemistry, Mineralogy, and biogenic structures. *Stratigr. Geol. Correl.* **30** (6), 475–497 (2022).
69. Lundgren, B. Studier ofver Fossilforande Losa block. *Geol. Stock Forh.* **13**, 111–121 (1891).
70. Dahmer, G. Lebensspuren Aus dem Taunusquarzit und Den siegener schichten (Unterdevon). *Preussischen Geologischen Landesanstalt Zu Berlin Jahrbuch*. **57**, 523–539 (1937).
71. Mägdefrau, K. Über einige Bohrgänge Aus dem unteren muschelkalk von Jena. *Paläontologische Z.* **14**, 150–160 (1932).
72. Frey, R. W., Howard, J. D. & Pryor, W. A. *Ophiomorpha*: its morphologic, taxonomic, and environmental significance. *Palaeogeogr. Palaeoclimatol. Palaeoecol.* **23**, 199–229 (1978).
73. Knaust, D. The ichnogenus *Ophiomorpha*: taxonomy and environmental distribution. *Earth Sci. Rev.* **261**, 104988 (2024).
74. Knaust, D. *Balanoglossites*-burrowed firmgrounds–the most common ichnofabric on earth? *Earth Sci. Rev.* **220**, 103747 (2021).

75. Chakraborty, P. P. & Bailwal, R. Architecture of a tide-influenced, wave dominated shallow-marine deposit from a paleoproterozoic rift setting: example from the Badalgarh Formation, Bayana basin, Rajasthan, Northwest India. *J. Earth Syst. Sci.* **130**, 1–22 (2021).
76. Luan, X., Sproat, C. D., Jin, J. & Zhan, R. Depositional environments, hematite–chamosite differentiation and origins of middle ordovician iron ooids in the upper Yangtze region, South China. *Sedimentology* **71** (7), 2210–2247 (2024).
77. Mount, J. F. Mixing of siliciclastic and carbonate sediments in shallow shelf environments. *Geology* **12** (7), 432–435 (1984).
78. Sarkar, S. et al. Siliciclastic–carbonate mixing modes in the river-mouth bar palaeogeography of the upper cretaceous Garudamangalam sandstone (Ariyalur, India). *J. Palaeogeography*. **3** (3), 233–256 (2014).
79. Moore, D. M. & Reynolds, R. J. *X-ray Diffraction and the Identification and Analysis of Clay Minerals*. (1989).
80. Banerjee, S., Farouk, S., Nagm, E., Choudhury, T. R. & Meena, S. S. High mg-glauconite in the Campanian Duwi formation of Abu Tartur plateau, Egypt and its implications. *J. Afr. Earth Sc.* **156**, 12–25 (2019).
81. Thompson, G. R. & Hower, J. The mineralogy of glauconite. *Clays Clay Miner.* **23** (4), 289–300 (1975).
82. López-Quirós, A. et al. Glaucony authigenesis, maturity and alteration in the Weddell sea: an indicator of paleoenvironmental conditions before the onset of antarctic glaciation. *Sci. Rep.* **9** (1), 13580 (2019).
83. Rudmin, M., Banerjee, S., Mazurov, A., Makarov, B. & Martemyanov, D. Economic potential of glauconitic rocks in Bakchar deposit (SE Western Siberia) for alternate potash fertilizer. *Appl. Clay Sci.* **150**, 225–233 (2017).
84. Porrenga, D. H. Non-marine glauconitic illite in the lower oligocene of Aardebrug, Belgium. *Clay Miner.* **7** (4), 421–430 (1968).
85. Bansal, U., Pande, K., Banerjee, S., Nagendra, R. & Jagadeesan, K. C. The timing of oceanic anoxic events in the cretaceous succession of cauvery basin: constraints from $^{40}Ar/^{39}Ar$ ages of glauconite in the Karai shale formation. *Geol. J.* **54** (1), 308–315 (2019).
86. Kelly, J. C. & Webb, J. A. The genesis of glaucony in the Oligo–Miocene Torquay Group, southeastern australia: petrographic and geochemical evidence. *Sed. Geol.* **125** (1–2), 99–114 (1999).
87. Tribovillard. et al. Syndepositional glauconite as a paleoenvironmental proxy-the lower cenomanian chalk of cap blanc Nez (N-France). *Chem. Geol.* **584**, 120508 (2021).
88. Tribovillard et al. The contrasting origins of glauconite in the shallow marine environment highlight this mineral as a marker of paleoenvironmental conditions. *Comptes Rendus Géoscience*. **355** (S2), 1–16 (2023).
89. Mandal, S., Banerjee, S., Sarkar, S., Mondal, I. & Choudhury, T. R. Origin and sequence stratigraphic implications of high-alumina glauconite within the lower Quartzite, Vindhyan supergroup. *Mar. Pet. Geol.* **112**, 104040 (2020).
90. Mandal, S., Choudhury, T. R., Das, A., Sarkar, S. & Banerjee, S. Shallow marine Glauconitization during the proterozoic in response to intrabasinal tectonics: A study from the proterozoic lower Bhander Sandstone, central India. *Precambrian Res.* **372**, 106596 (2022).
91. Mohammed, I. Q. et al. The influence of depositional conditions on chemical and mineralogical composition of glauconite: case study from the late cretaceous Dokan basin in Kurdistan region of Iraq. *Appl. Clay Sci.* **263**, 107639 (2025).
92. Burst, J. F. Mineral heterogeneity in glauconite pellets. American mineralogist. *J. Earth Planet. Mater.* **43** (5–6), 481–497 (1958).
93. Odin, G. S. & Fröhlich, F. Glaucony from the kerguelen plateau (Southern Indian Ocean). *Developments Sedimentology*. **45**, 277–294 (1988).
94. Odin, G. S. & Fullagar, P. D. Geological significance of the glaucony facies. *Developments Sedimentology*. **45**, 295–332 (1988).
95. Courbe, C., Velde, B. & Meunier, A. Weathering of glauconites: reversal of the Glauconitization process in a soil profile in Western France. *Clay Minerals*. **16** (3), 231–243 (1981).
96. Ireland, B. J., Curtis, C. D. & Whiteman, J. A. Compositional variation within some glauconites and illites and implications for their stability and origins. *Sedimentology* **30** (6), 769–786 (1983).
97. Jach, R. & Starzec, K. Glaucony from the condensed Lower-Middle jurassic deposits of the Križna Unit, Western Tatra Mountains, Poland. *Ann. Soc. Geol. Pol.* **73**, 183–192 (2003).
98. Longuépée, H. & Cousineau, P. A. Constraints on the genesis of Ferrian illite and aluminum-rich glauconite: potential impact on sedimentology and isotopic studies. *Can. Mineral.* **44** (4), 967–980 (2006).
99. Velde, B. The chemical evolution of glauconite pellets as seen by microprobe determinations. *Mineralogical Magazine*. **40**, 753–760 (1976).
100. Velde, B. *Clay Minerals: A Physico-Chemical Explanation of their Occurrence* (Elsevier, 1985).
101. Isson, T. T. & Planavsky, N. J. Reverse weathering as a long-term stabilizer of marine pH and planetary climate. *Nature* **560** (7719), 471–475 (2018).
102. Choudhury, T. R., Khanolkar, S. & Banerjee, S. Glauconite authigenesis during the warm Climatic events of paleogene: case studies from shallow marine sections of Western India. *Glob. Planet Change*. **214**, 103857 (2022).
103. Bansal, U., Banerjee, S., Pande, K., Arora, A. & Meena, S. S. The distinctive compositional evolution of glauconite in the cretaceous Ukra hill member (Kutch basin, India) and its implications. *Mar. Pet. Geol.* **82**, 97–117 (2017).
104. Bansal, U., Banerjee, S., Ruidas, D. K. & Pande, K. Origin and geochemical characterization of the glauconites in the upper cretaceous Lameta Formation, Narmada Basin, central India. *J. Palaeogeography*. **7** (2), 99–116 (2018).
105. Ekdale, A. A. & Mason, T. R. Characteristic trace-fossil associations in oxygen-poor sedimentary environments. *Geology* **16** (8), 720–723 (1988).
106. Moffitt, S. E. et al. Paleoceanographic insights on recent oxygen minimum zone expansion: lessons for modern oceanography. *PloS One*. **10** (1), 0115246 (2015).
107. Schönfeld, J. et al. Records of past mid-depth ventilation: cretaceous ocean anoxic event 2 vs. Recent oxygen minimum zones. *Biogeosciences* **12** (4), 1169–1189 (2015).
108. Wong, J. C. et al. Do phytoplankton require oxygen to survive? A hypothesis and model synthesis from oxygen minimum zones. *Limnol. Oceanogr.* **68** (7), 1417–1437 (2023).
109. Föllmi, K. B. Early cretaceous life, climate and anoxia. *Cretac. Res.* **35**, 230–257 (2012).
110. Schlanger, S. O. & Jenkyns, H. Cretaceous oceanic anoxic events: causes and consequences. *Geologie En Mijnbouw* **55**(3–4), 179–184 (1976).
111. Metzner, N., Wilmsen, M. & Böning, P. Greensand formation, siliceous Earth deposition and coastal metal drawdown in the Danubian cretaceous basin (Bavaria, Germany). *Mar. Pet. Geol.* **170**, 107067 (2024).
112. Xu, Z. et al. Enhanced terrigenous organic matter input and productivity on the Western margin of the Western Pacific warm pool during the quaternary sea-level lowstands: forcing mechanisms and implications for the global carbon cycle. *Q. Sci. Rev.* **232**, 106211 (2020).
113. Taylor, A. M. & Goldring, R. Description and analysis of bioturbation and ichnofabric. *J. Geol. Soc.* **150** (1), 141–148 (1993).

Acknowledgements

The authors acknowledge the financial support from the Centre of Excellence in Oil, Gas and Energy through the sponsored project DO/2021-COGE002-015 (High-resolution sequence stratigraphic interpretations of Cretaceous succession of Jaisalmer Basin and its implication for reservoir characterization) and collaborating PSUs ONGC Ltd, OIL, and BPRL. Arpita Chakraborty (PMRF ID: 1302641) expresses gratitude to the Ministry of Education, New Delhi, Government of India, for granting the Prime Minister's Research Fellow (PMRF) scheme. The authors thank the Department of Science and Technology, Government of India, for the FEG-SEM facility

at the Department of Earth Sciences, IIT Bombay, through the FIST grant no. SR/FST/ES-II/2019/63. All the authors thank the Indian Institute of Technology (IIT), Bombay, for providing technical infrastructure support. The authors extend their gratitude to Prof. S.C. Patel and Javed M. Shaikh for allowing and assisting with mineral analyses through the EPMA, a national facility in the Department of Earth Sciences, IIT Bombay. The authors are thankful to Zhaokai Xu and two anonymous reviewers, and the Editor for their constructive criticisms of an earlier version of the manuscript.

Author contributions

AC, AS, BS: Wrote the main paper, AC prepared Figs. 1, 2, 5, 6 and 7, and Supplementary data, AS Prepared Figs. 3 and 4, BS: prepared Plate 1. SB, SDG, and JP supervised the work; All authors reviewed the manuscript.

Declarations

Competing interests

The authors declare no competing interests.

Additional information

Supplementary Information The online version contains supplementary material available at https://doi.org/10.1038/s41598-025-21056-9.

Correspondence and requests for materials should be addressed to S.B.

Reprints and permissions information is available at www.nature.com/reprints.

Publisher's note Springer Nature remains neutral with regard to jurisdictional claims in published maps and institutional affiliations.